Cerebral Cortex December 2011;21:2704–2711
doi:10.1093/cercor/bhr059
Advance Access publication April 28, 2011

Automated Analysis of Spines from Confocal Laser Microscopy Images: Application to the Discrimination of Androgen and Estrogen Effects on Spinogenesis

Hideo Mukai[1,2,3,4], Yusuke Hatanaka[1], Kenji Mitsuhashi[1], Yasushi Hojo[1,2,3], Yoshimasa Komatsuzaki[1], Rei Sato[1], Gen Murakami[1,2,3], Tetsuya Kimoto[1,2,3] and Suguru Kawato[1,2,3]

[1]Department of Biophysics and Life Sciences, Graduate School of Arts and Sciences, [2]Bioinformatics Project, Japan Science and Technology Agency, [3]Core Research for Evolutional Science and Technology of Japan Science and Technology Agency, The University of Tokyo, Meguro, Tokyo 153-8902, Japan and [4]Department of Integrative Sciences in Physics and Biology, College of Humanities and Sciences, Nihon University, Setagaya, Tokyo 156-8550, Japan

Address correspondence to Suguru Kawato, Department of Biophysics and Life Sciences, Graduate School of Arts and Sciences, The University of Tokyo, 3-8-1 Komaba, Meguro, Tokyo 153-8902, Japan. Email: kawato@phys.c.u-tokyo.ac.jp.

Accurate 3D determination of postsynaptic structures is essential to our understanding memory-related function and pathology in neurons. However, current methods of spine analysis require time-consuming and labor-intensive manual spine identification in large image data sets. Therefore, a realistic implementation of algorithm is necessary to replace manual identification. Here, we describe a new method for the automated detection of spines and dendrites based on analysis of geometrical features. Our "Spiso-3D" software carries out automated dendrite reconstruction and spine detection using both eigenvalue images and information of brightness, avoiding detection of pseudo-spines. To demonstrate the potential application of Spiso-3D automated analysis, we distinguished the rapid effects of androgen and estrogen on rapid modulation of spine head diameter in the hippocampus. These findings advance our understanding of neurotrophic function of brain sex steroids. Our method is expected to be valuable to analyze vast amounts of dendritic spines in neurons in the mammalian cerebral cortex.

Keywords: automatic detection, hippocampus, steroids, synapse, spine

Introduction

Dendritic spines (i.e., postsynaptic structures) of neurons form synaptic contacts that are involved in neuronal computational processes. Visualization and analysis of spines is of critical importance to elucidate physiological changes of morphological plasticity (Matsuzaki et al. 2004; Harvey et al. 2008), as well as effects of various hormones and pharmacological agents (Mukai et al. 2007; Ogiue-Ikeda et al. 2008).

The combination of laser-scanning confocal microscopy/2-photon microscopy and fluorescent dye has allowed us to collect large bodies of neuronal image data (van Pelt et al. 2001), namely tens of dendrites and several tens of thousands of spines residing on dendrites of a single neuron.

Conventional methods using manual tracing software such as Neurolucida (MicroBrightField) are time-consuming and are not suitable for the analysis of large data sets. Recently a number of techniques with varying degrees of automation have been introduced (Dima et al. 2002; Streekstra and van Pelt 2002; Al-Kofahi et al. 2003; He et al. 2003). However, most of those studies are devoted to extracting the dendrites from neuronal images. Manual counting of spines is the most time-consuming part of the entire analysis and has not been yet replaced by an efficient automated measure. Therefore, introduction of a new automatic analysis of neuronal structure including spines will greatly enhance progress of research in the area.

Here, we developed a new software, Spiso-3D, to extract spines as well as dendrites in neuronal image based on their geometrical features (Lindeberg 1990; Schmitt et al. 2004), a completely different approach to the ray-bursting method (Wearne et al. 2005; Rodriguez et al. 2008). Our "geometric method" utilizes scale-free shape-dependent analysis, making it less dependent on brightness in the image. For example, spines are located by pixels that have negative products of eigenvalues calculated from the Hessian matrix of the image. On the other hand, the ray-bursting method mainly exploits information of brightness to define boundaries of dendrites and spines. As Spiso-3D is a Java-based program, it will readily operate on a PC using relatively limited computational resources. Furthermore, here we demonstrate the successful application of Spiso-3D to the analysis of the different effects elicited by androgen and estrogen on spinogenesis of hippocampal neurons.

Materials and Methods

Experimental Protocols

Animals

Adult male Wistar rats (3 months old) were purchased from Saitama Experimental Animals Supply (Japan). The experimental procedure of this research was approved by the Committee for Animal Research of the University of Tokyo.

Acute Hippocampal Slices and Treatments with Sex Steroids

Adult male rats were deeply anesthetized with ethyl ether and decapitated. The left hippocampus is removed from the brain and placed in artificial cerebrospinal fluid (ACSF) at 4 °C. ACSF consisted of (mM): 124 NaCl, 5.0 KCl, 1.25 NaH_2PO_4, 2.0 $MgSO_4$, 2.0 $CaCl_2$, 22 $NaHCO_3$, 10 glucose and was equilibrated with 95% O_2/5% CO_2. Hippocampal slices of 400 μm thick are prepared with a vibratome (Dosaka). Slices are then transferred into an incubating chamber containing ACSF held at 25 °C for 2 h for recovery. These acute slices were then incubated with testosterone, dihydrotestosterone, or estradiol (Sigma) for 2 h. Slices were then prefixed with 4% paraformaldehyde in phosphate-buffered saline at 4 °C for 2–4 h.

Visualization of Neuronal Cells by Fluorescent Dye

Neurons in hippocampal slices were visualized by injection of Lucifer Yellow under a microscope (E600FN, Nikon) equipped with an infrared camera (C2400–79H, Hamamatsu Photonics) and with a 40× water immersion lens (Nikon). Dye injection was performed with a glass electrode whose tip is filled with 5% Lucifer Yellow for 15 min, using

Axopatch 200B (Axon Instruments). Approximately 5 neurons within 100–200 μm depth from the surface of slice were injected. Slices were then fixed again with 4% paraformaldehyde overnight.

Imaging with Confocal Laser Microscopy

The imaging was performed from sequential *z*-series scans with LSM5 PASCAL confocal microscope (Carl Zeiss) or equivalent microscope at high zoom (3.0) with a 63× water immersion lens, NA 1.2 (Zeiss). The applied zoom factor (3.0) yield 23 pixels per 1 μm. The confocal lateral resolution was approximately 0.26 μm. The resolution limits are regarded to be sufficient to allow the determination of the density of spines. For Lucifer Yellow, the excitation and emission wavelengths were 488 nm and 515 nm, respectively. For analysis of spines, 3D image was reconstructed from approximately 40 sequential *z*-series sections of every 0.45 μm. Confocal images were then deconvoluted using AutoDeblur software (MicroCybernetics). To perform unbiased selection of hippocampal CA1 neurons, somas of neurons were sampled along pyramidal layers with the optical fractionation, in which they are apart by roughly 200 μm. Dendrites were selected with concentric spherical probes centered on the soma (modified Sholl analysis). We selected secondary dendrites in the stratum radiatum lying between 100 and 250 μm from the soma because in hippocampal CA1 pyramidal neurons, sex-steroid effects are most prominent in these secondary dendrites (100–200 μm apart from the soma) rather than basal dendrites in the stratum oriens or apical dendrites in the lacunosum-moleculare (Murakami et al. 2006). Typically in total, 25–60 dendritic segments (50–80 μm length) from 12–30 neurons in 6–15 slices from 3–5 animals, and total 1200–3500 spines were analyzed for each experimental condition. Density and morphology of dendritic spines were analyzed by tracing neurons with Spiso-3D.

Semiautomated Detection by Spiso-3D

Desired machine resource is as follows: A PC-AT compatible with CPU: Intel Pentium 4 (clock speed 3.2 GHz); RAM: 3 GB or higher, OS: Windows XP and Windows 7. All programs are written in Java (ver 6.1) and Java 3D under developmental environment Eclipse (Sun Microsystems). Memory available for Eclipse should be allocated at 1.44 GB (maximum) to ensure smooth calculation. After launching Eclipse, Spiso program is started by selecting the program name that appears under "Run."

Setting Parameters

Entering parameters is necessary for following calculation. Scale factors for confocal image (e.g., micrometers per pixel in *X*–*Y*–*Z* direction) are entered by the user here.

Creating Max XY Projection of the Image

Opening the deconvoluted confocal image (must be converted into tiff), press the button "Max XY." The images are integrated in *Z* direction and Max XY projection image appears on the screen.

Tracing the Dendrite

Appropriate scale factor for dendrite tracing is then selected (σ in Fig. 5). Typical value for σ is 2.4. Pressing the bar "dendrite," elapsed time is indicated on the screen. Typical analysis time is a few minutes for an image with 20–30 stacks of 1024 × 300 pixels. After several iterations of the process the best-fit results are obtained (Fig. 6*A*). In some cases, disconnected dendrites are obtained as a result, then connect the dendrites manually to single dendrite.

Locating Spines

After changing the tab for "spine," setting the parameters for spine is done here (sensitivity is S in Fig. 3). Pressing the bar "spine," elapsed time is indicated on the screen. Typical analysis time is several minutes for an image with 20–30 stacks of 1024 × 300 pixels. The process will be iterated until the best-fit results are obtained (Fig. 6*B*). While counting the spines in the reconstructed images, the correction of position and verification of spines were aided by observation of the images in consecutive *Z* stacks. If necessary, position and/or diameters of spines can be manually corrected (Fig. 6*C*).

Displaying Fitted Parameters

In addition to images superimposed with the fitted dendrites and spines, the results obtained by Spiso can be exported to an Excel format (Supplementary Fig. S1). The results include the density of spines on the dendrite and the distribution of spines classified by spine head diameter.

If desired, 3D image of reconstructed dendrite with spines can be shown in another window.

Results and Discussion

Theoretical Results

Scale Transformation

We employed scale-free analysis using scale-space transformation. Scale-space analysis smoothes noise and structures smaller than objects of interest by convoluting images with a scale factor (σ) in Gaussian kernel (for theoretical description, see Lindeberg 1990 or Schmitt et al. 2004).

$$I*K(\sigma)=\int I(x)\exp(-(x-x')^2/2\sigma^2)\mathrm{d}x',$$

$$K(\sigma)=N\exp(-(x-x')^2/2\sigma^2).$$

For dendrites, a scale factor of 0.5–2 μm was used, while for spines, a scale factor of 0.01–0.2 μm was used.

Dendrite Tracing

Following scale transformation, the dendritic structure was extracted from the 3D image by tracing. Using a Max XY projection image generated from a stack of confocal images, the centeredness of the dendrite was calculated and connected to form a linear structure. To this end, the total brightness function $f(\mathbf{x})$ in the Max XY projection image is expanded using polynominals in divided lattices within the linear structure (Krissian et al. 2000).

Then a series of peaks of the brightness function $f(\mathbf{x})$ are found, called the ridge line. On the ridge line, $O(\mathbf{x}_1)$ is given an extremum of $f'(\mathbf{x}_1) = 0$ or $-\lambda_{max}$ because the gradient of the tangential direction of the ridge line should be zero and derivatives in normal direction must be negative, taking a local maximum. By connecting these peaks, the center line of the dendrite can be obtained.

Next, the diameter of nodes in the dendrite was calculated from the image. Equally distant points for both side A and B from the point of $\mathbf{x}_1$ in normal direction of the center line of the dendrite are found and unit vectors OA and OB are drawn. To determine the boundary of the dendrite, then τ, the boundary product for $\mathbf{e}_{OA}$, $\mathbf{e}_{OB}$,

$$\tau=(-\mathbf{e}_{OA}\cdot\mathrm{grad}\,f_A)\cdot(-\mathbf{e}_{OB}\cdot\mathrm{grad}\,f_B),$$

can be defined (Fig. 1).

The distance from point O to A(r) or B(r), is changed within the range of 0.1–5.0 μm, yielding boundary product τ(r). Among peaks of τ(r), the nearest peak to the center point O is defined as the end point of the diameter of the node. The diameter of the node should be obtained by doubling the distance between the end point and the center point O.

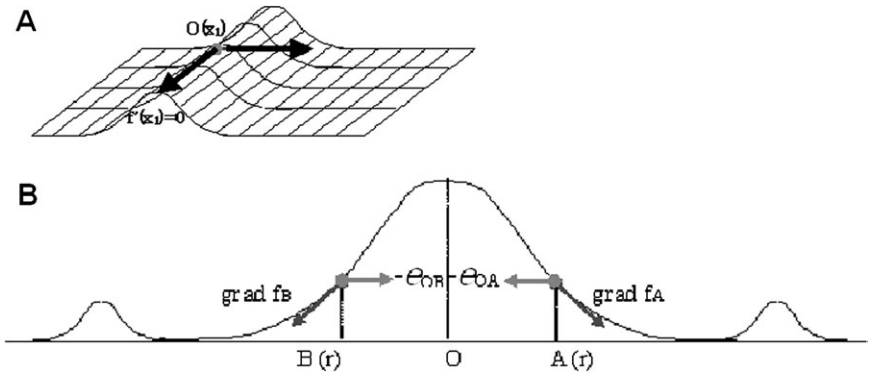

Figure 1. Procedures for tracing dendrite. (*A*) Finding dendrite nodes using ridge line, the series of peaks, of brightness ($\mathbf{x}_1$) function. On the ridge line, $O(\mathbf{x}_1)$ should give an extremum of $f'(\mathbf{x}_1) = 0$ or $-\lambda_{max}$ because in tangential direction of the ridge line the gradient should be zero. (*B*) Equally distant points for both side A and B from the point of $\mathbf{x}_1$ in normal direction of the center line of the dendrite are found and unit vectors OA and OB are drawn. Then τ, boundary product for $\mathbf{e}_{OA}$, $\mathbf{e}_{OB}$, can be calculated (see text).

Reconstruction of 3D Dendrite by Pattern Matching

To reconstruct the dendrite 3-dimensionally, dendrite nodes from Max XY projection are pattern-matched with *XY* in the *Z* direction (Z_j). The pixel brightness at the center of each node (X_p, Y_p) is compared in all images. The node center is assigned to the Z_m plane, where maximum pixel brightness at (X_k, Y_k) is observed. The diameter of dendrite node in 3D is the same as the diameter of the dendrite node determined in Max XY projection. After matching all nodes, matched nodes are connected, thereby 3-dimensionally reconstructing the dendrite.

Spine Determination

To determine spines, we use Hessian tensor that is obtained as second derivatives from Taylor expansion of the spine brightness function $I(\mathbf{x})$. The spine brightness function is obtained after subtraction of the traced dendrite from $f(\mathbf{x})$. $I(\mathbf{x})$ can be expressed in the following via Taylor expansion:

$$I(\mathbf{x}+\varepsilon\mathbf{u}) = I(\mathbf{x}) + \varepsilon I'(\mathbf{u}) + \tfrac{1}{2}\varepsilon^2 I''(\mathbf{u}) + \cdots = I(\mathbf{x}) + \varepsilon \cdot \mathrm{grad} I \cdot \mathbf{u} + \tfrac{1}{2}\varepsilon^2 \mathbf{u}^t \mathbf{H} \mathbf{u} + \cdots$$
$$= I(\mathbf{x}) + \varepsilon(g_+ u_+ + g_- u_-) + \tfrac{1}{2}\varepsilon^2(\lambda_+ u_+^2 + \lambda_- u_-^2) + \cdots$$

with

$$\mathrm{grad} I = \begin{pmatrix} \frac{\partial I}{\partial x} \\ \frac{\partial I}{\partial y} \end{pmatrix}, \quad H = \begin{pmatrix} \frac{\partial^2 I}{\partial x^2} & \frac{\partial^2 I}{\partial x \partial y} \\ \frac{\partial^2 I}{\partial y \partial x} & \frac{\partial^2 I}{\partial y^2} \end{pmatrix}, \quad \mathrm{diag} H = \begin{pmatrix} \lambda_+ & 0 \\ 0 & \lambda_- \end{pmatrix},$$

where $\mathbf{u}$ is a unit vector of direction; λ_+ and λ_- ($\lambda_+ > \lambda_-$) are the eigenvalues of diagonalized Hessian tensor; and g_+ and g_- are the corresponding derivatives of direction for λ_+ and λ_- (u_+ and u_-, respectively).

Candidate points of the spine head are extracted as points where both λ_+ and λ_- yield negative values since it is assumed that the spine head is an isolated closed volume with a closed surface. The thin spine neck is considered negligible due to very weak brightness. Note that negative eigenvalues of Hessian tensor (λ_+ and λ_-) represent the negative curvature of closed spine surface.

The spine center and diameter are determined by merging the gradient vector image of spine center candidate points with the image of calculated spine diameters. Spines are approximated by a disk with the longest diameter as detailed below.

Locating the Spine Center

From Taylor expansion of the brightness function $I(\mathbf{x})$, we obtain grad $I(\mathbf{x})$ and Hessian tensor $\mathbf{H}$. In the pixels that both eigenvalues of $\mathbf{H}$ are negative, the inner product of grad I which shows degree of facing of 2 vectors, is calculated,

$$\phi_A = (\mathrm{grad} I_{A+1}) \cdot (\mathrm{grad} I_{A-1})$$

where A + 1 and A – 1 is the 4 nearest neighbors in X or Y direction of pixel A (x,y) (Fig. 2). Pixels with at least one in 4 negative φ_A values are stored as candidates for the spine center point.

The above procedures are iterated for $0.01 < \sigma < 2.0$ at step of 0.01. One spine area consists of many candidate points for spine center (Fig. 2*D*,*E*). The candidates for spine center are collected as spine center detection image, which is then digitized as the distance image (Fig. 2*F*). To create the digitized distance image, the minimum number of pixels to reach the center pixel from perimeter pixels is assigned on each pixel. The perimeter (edge) pixel is assigned to be 1. The true center C of spine can be determined as the pixel that has a maximum number (Fig. 2*F*). In this way, the spine center detection is carried out for each slice plane.

Determination of Spine Diameter

Once candidates for the spine center point are determined, a "radius detection image" showing the putative spine region is created, which we use to calculate the spine radius. To generate the radius detection image, we first calculate ||grad I_A||, the norm of grad I_A, at the point where 2 eigenvalues of diagonalized Hessian tensor are both negative. Pixels with nonzero ||grad I_A|| are regarded as candidate spine region points (Fig. 3). These procedures are iterated for $0.01 < \sigma < 2.0$ at step of 0.01. Identified candidate spine region points are assembled into radius detection image which is then digitized to create the distance image. To create the distance image, the minimum number of pixels to reach the center pixel from the perimeter pixels is assigned on each pixel (Fig. 3*E*). Finally, spine diameter is determined by combining the spine center detection image (Fig. 2*F*) with Fig. 3*E*, by superimposing both the center Cs. The combined image is again digitized to create the distance image. The maximum distance number R (assigned for the center C) is adopted as a spine radius (a spine diameter $D = 2R$) (Fig. 3*F*). The same procedure is carried out for each Z stack of slice (Z_i; e.g., XY plane). However, since distances allocated to each pixel (1,2,3,...) are not precise enough, the calculated radius value is adjusted. If at least one of the adjoining 8 neighboring pixels of the pixel with the maximum

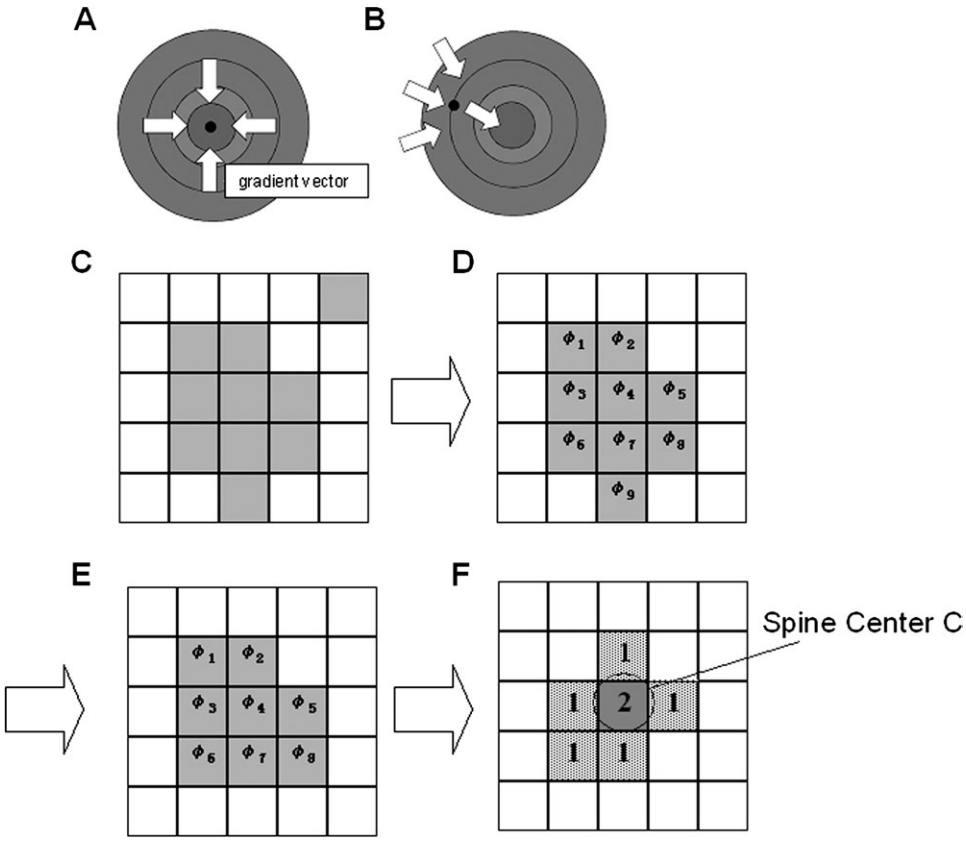

Figure 2. Procedures for locating spine center. (*A*) A schematic illustration of the pixel P(*x*,*y*) that is a true spine center. Four nearest neighbors in *X* or *Y* direction with all φ_A are negative. (*B*) P(*x*,*y*) that is not a true spine center with one positive φ_A. (*C*) A schematic example of gradient vector image. Gray tiles indicate pixels of spine center candidate, that is, $||\text{grad } I_A|| > 0$, white tiles are pixels with grad $I_A = 0$. (*D*) Calculation of the inner product of gradient vectors φ at pixels where λ_1 and λ_2 are both negative. (*E*) Spine center detection image created by selecting pixels with negative φ_A. (*F*) Digitized spine center detection image. In spine center candidates, minimum number of pixels to reach the center pixel from perimeter (edge) pixel is counted and assigned on each pixel. A perimeter pixel has a value of 1. The pixel having maximum number $r_c = 2$ is of the spine center C.

R also have the value *R*, then *R* is unadjusted, however, if all 8 neighboring pixels have the value of *R* minus 1 (*R* – 1), the radius is adjusted to *R* minus 0.5 (*R* – 0.5). With this standard, we attempted to reflect various shapes of spines, which are difficult to approximate by using circles to model the spine.

Integration of Spines in 3D Direction

Once spine diameters are determined for each stack $XY(Z_i)$, identified spines along *Z* axis originally belonging to the same spine are grouped 3-dimensionally (Fig. 4). Identified spines whose center-to-center distance are less than R_j (j stands for Z_j) with overlap of at least one pixel in *XY* brightness are assigned as the same spine. If the overlaps of brightness in spine regions along *Z* direction are separated more than 2 stacks (1 μm in physical distance in the current study), they are considered to belong to different spines. Then, the gravity center is taken as a new spatially weighted spine center.

$$O = \frac{\sum_i r_i x_i}{\sum_i r_i}$$

The largest radius within the group is adopted as a spine radius.

$$R_{\max} = \max(R_1, R_2, \ldots, R_n)$$

Accordingly, the diameter of spine is $D = 2R_{\max}$.

The entire analysis process of a dendrite and its spines are summarized in Fig. 5. The obtained results of the dendrite and spine analysis can be exported to an Excel format (Supplementary Fig. S1).

Final Manual Correction of Spines

The calculated spine is displayed on each plane as a circle overlaid on the original image with diameter $D = 2R_{\max}$ (Fig. 6). Typically, a small fraction of identified spines need manual correction of diameters (<15%). The diameter of spine in the reconstructed image is corrected by observation of the original image in consecutive single plane and adjusting the $R_{\max}$ radius of the calculated result to the original image. Some pseudo-spines may be detected (<2%) since spines typically have a neck shorter than 6 μm, pseudo-spines are erased if they are further than 8 μm from the dendritic center.

Our method of spine identification can also detect filopodium, a form of dendritic protrusions found in neurons at the developmental stage of the brain, which lacks an apparent head (0.1 – 0.2 μm). Filopodium can also be easily excluded by manual inspection since the population of filopodia may be less than 1% of the total spines in the adult brain.

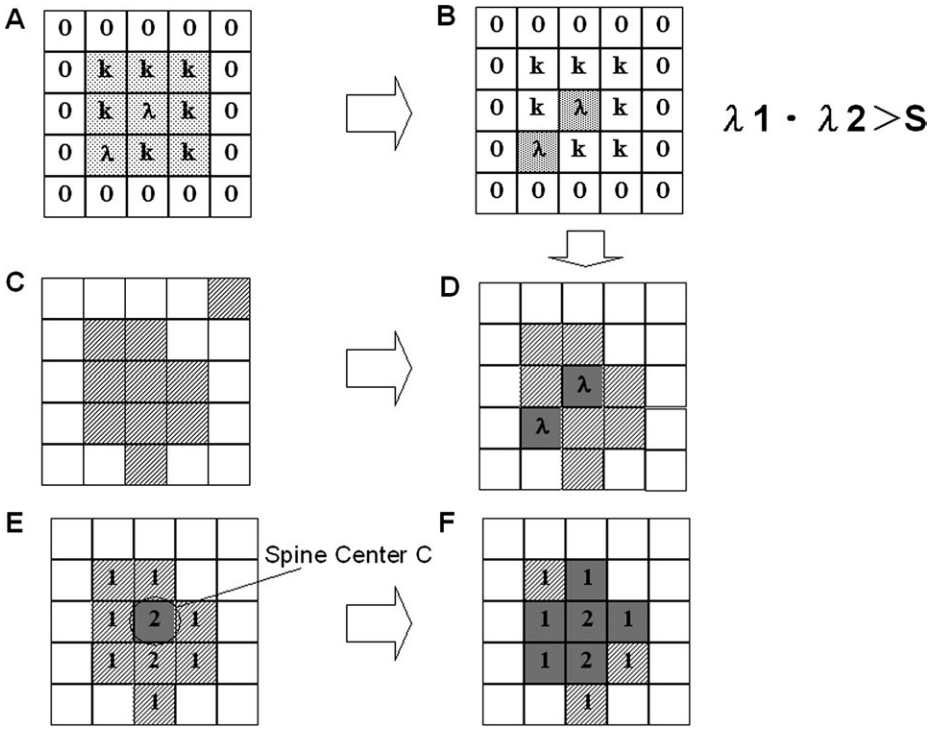

Figure 3. Spine diameter determination. (*A*) Spine center detection image. Eigenvalues of Hessian matrix are calculated at each pixel. "λ" indicates a pixel where 1) eigenvalues λ_1 and λ_2 are both negative and 2) $\lambda_1\lambda_2 > S$ (S: sensitivity set in the Spiso program by user). "k" indicates pixel with $\lambda_1\lambda_2 \leq S$. (*B*) Image of information of spines. "λ" pixels are marked for spine center candidates, while "k" pixels are omitted. (*C*) Gradient vector image in Figure 2*C*. (*D*) By superimposing (*B*) and (*C*), the connected area in gradient vector image with "λ" pixel inside is defined as "spine." The spine pixels are indicated as stripe pixels. (*E*) The radius detection image. To create the digitized distance image, the minimum number of pixels to reach the center pixel from the perimeter pixel is assigned on each pixel. (*F*) Spine diameter is determined by combining the spine center detection image (Fig. 2*F*) with Figure 3*E*, by superimposing both center C. The combined area is again digitized to create the distance image. The maximum distance number *R* (assigned for the center C) is adopted as a spine radius (a spine diameter $D = 2R$).

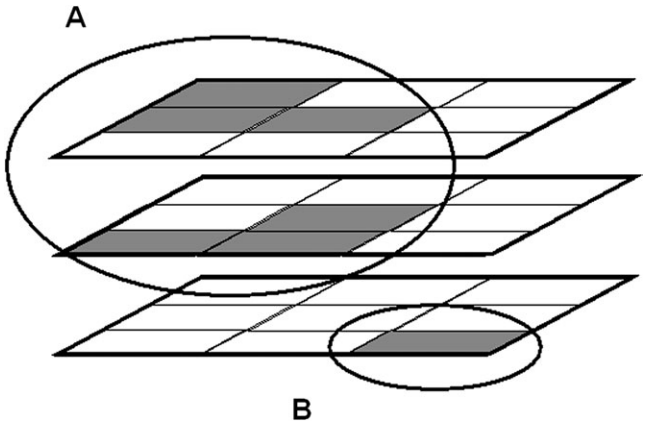

Figure 4. Integration of spines. Spines found on each plane along *Z* axis originally belonging to the same spine are grouped 3-dimensionally. If XY brightness overlaps at least one pixel, and spines whose distance between centers are less than R_j (j stands for Z_j) is assigned as the same spine. For example, the spines within circle A in this figure are grouped as one spine. If the overlaps of brightness in spine regions along *Z* direction are separated more than 2 stacks (1 μm in physical distance in the current study, e.g., spine area within circle B), they are considered to belong to another spine.

Less than a 2% difference in spine assessment was observed using our described automated methods compared with manual counting using Neurolucida (e.g., one of 50 spines along one sampled dendrite) (see Fig. 7).

Spine Neck Length Calculation

Neck length of each spine can also be determined by using coordinates of the spine center and the center of dendrite node (Supplementary Fig. S2).

Demonstration Movie of Spiso-3D Action

A demonstration of Spiso-3D is provided in Supplementary Material.

Experimental Results

Successful Application of Spiso-3D to Distinguish the Different Effects of Androgen and Estrogen on Enhanced Spinogenesis in Hippocampal Neurons

Synaptic modulation of hippocampal neurons by neurosteroids has attracted much attention because of their effects on memory-related function (Baulieu 1997; Mukai et al. 2007; Ogiue-Ikeda et al. 2008). Interestingly, androgen and estrogen are endogenously synthesized in hippocampal neurons (Kawato et al. 2002; Hojo et al. 2004; Kretz et al. 2004), and they have rapid effects on synaptic plasticity (Mukai et al. 2007; Hatanaka et al. 2009). Using Spiso analysis on spine head diameter, we clearly distinguished the different effects of testosterone (T, 10 nM), dihydrotestosterone (DHT, 10 nM), and 17β-estradiol (E2, 1 nM) on dendritic spines of hippocampal CA1 pyramidal neurons in acute hippocampal slices (Fig. 7). These sex hormones rapidly (within 2 h) increased the total spine density from 0.97 spines/μm to 1.28 (T), 1.32 (DHT), and 1.34 (E2), respectively (Fig. 7*A*). While the effects of T, DHT,

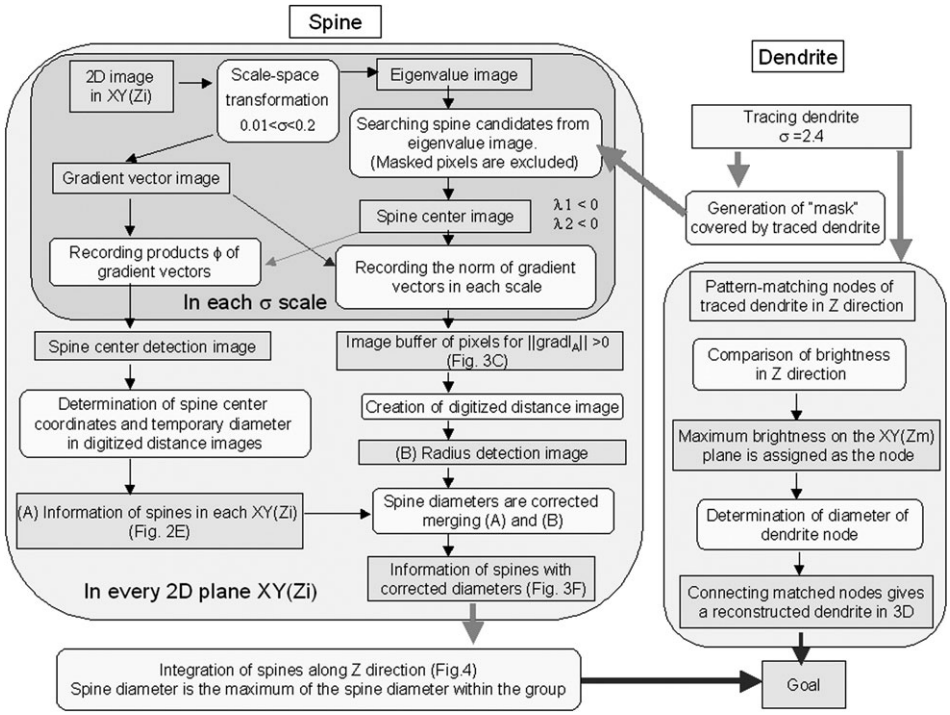

Figure 5. Summary of the spine analysis protocol. Left, Flow diagram of spine analysis. Right, Flow diagram of dendrite analysis. The 2 results are combined to yield a reconstructed dendrite with spines.

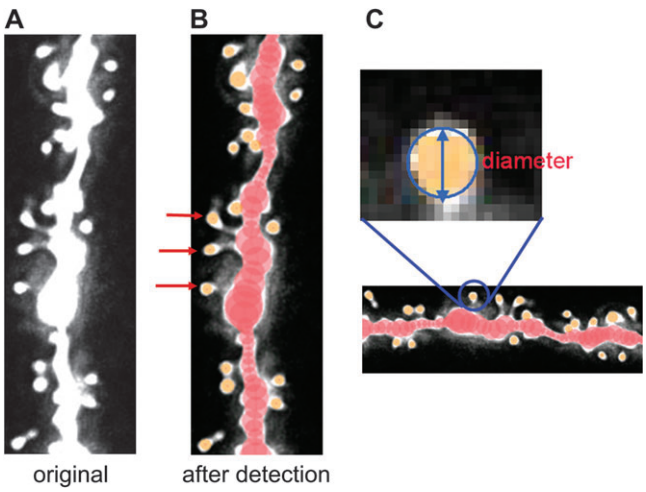

Figure 6. (*A*) Original image of dendrite. (*B*) Traced dendrite (connected series of red circles) and spines (yellow circles) superimposed on the image. (*C*) Calculated diameters of spines are superimposed on the spine images.

and E2 treatment on total spine density were indistinguishable, closer examination spine head diameter revealed marked differences in the distribution of spine head diameter between T, DHT, and E2 treatments (Fig. 7*B*,*C*). To distinguish different responses in spine subpopulations, spines were classified into 3 categories according to their head diameters: 1) a small-head spine, which has head diameter (*D*) between 0.2 and 0.4 μm, 2) a middle-head spine, which has head diameter between 0.4 and 0.5 μm, and 3) a large-head spine, which has head diameter between 0.5 and 1.0 μm.

DHT treatment was found to increase large- and middle-head spines, whereas T increased large- and small-head spines. In contrast, E2 treatment increased only small-head spines (Fig. 7*B*,*C*).

The observed differences in the effects of the hormones on spine subpopulations may have functional implications, for example, large-head spines may contain more α-amino-3-hydroxy-5-methyl-4-isoxazolepropionic acid (AMPA) receptors since spine-head size positively correlates with the density of AMPA-type glutamate receptors (Kopec et al. 2007; Shinohara et al. 2008). Since the induction of long-term potentiation (LTP) is dependent on the density of AMPA receptors in spines (Kopec et al. 2007; Shinohara et al. 2008), increased density of AMPA receptors in large-head spines could facilitate LTP. Increased density of large-head spines following DHT treatment could potentially facilitate LTP induction, in contrast to T, which only moderately increased large-head spines or E2 that had no effect on the density of large-head spines.

These findings demonstrate the importance of the consideration of spine diameter to distinguish different types of neurotrophic effects. Although manual determination of spine diameter is labor intensive, the newly developed Spiso-3D software provides a sensitive and specific method for the rapid automated determination of spine density. As a control, we also performed analysis of these spine data for T, DHT, and E2 using Neurolucida software, and we obtained results almost identical to those by Spiso-3D within 2% error (Fig. 7*D*). However, spine numbers might be underestimated or overestimated with Neurolucida, if one need to count very many spine numbers due to human counting error. Since the majority of spines (>95%) had a distinct head and neck, stubby spines (long filamentous protrusion with no distinguishable head, less than 3%), and filopodium (protrusion without a distinguishable head, less than 0.1%) did not significantly contribute to overall changes.

Our approach of automated spine analysis will be particularly useful for analysis of involvement of intracellular kinase signaling in spinogenesis, such as MAPK, PKA, PKC, PI3K, CaMKII, or calcineurin (Hatanaka et al. 2009) because considerable amount of data to analyze are necessary to

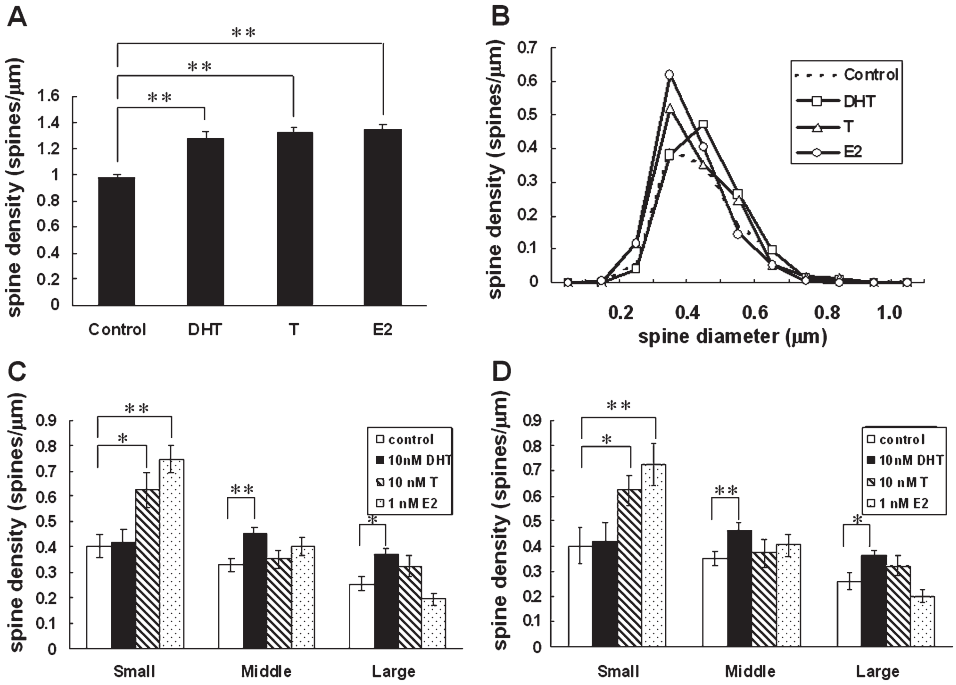

Figure 7. Effects of androgens and estrogens on changes in the density and morphology of spines. Spines were analyzed by Spiso-3D along the secondary dendrites in the stratum radiatum of CA1 pyramidal neurons. (*A*) Total spine density. Vertical axis is the average number of spines per 1 μm. A 2-h treatment in ACSF without hormone (Control, 0.98 spines/μm), with 10 nM dihydrotestosterone (DHT, 1.28 spines/μm) with 10 nM testosterone (T, 1.32 spines/μm), with 1 nM estradiol (E2, 1.34 spines/μm). (*B*) Histogram of spine head diameters. Abbreviations are same as in (*A*). Vertical axis is the number of spines per 1 μm of dendrite. After a 2-h treatment in ACSF without steroids (Control, dashed line), DHT (open square), T (open triangle), and E2 (open circle). (*C*) Density of 3 subtypes of spines with dihydrotestosterone (DHT), testosterone (T), and estradiol (E2) analyzed by Spiso-3D. Abbreviations are same as in (*A*). Vertical axis is the average number of spines per 1 μm of dendrite. From left to right, ACSF without hormones (open column), 10 nM DHT (filled column), 10 nM T (stripe column), and 1 nM E2 (dotted column). Spine density (spines/μm) of each subclass is as follows: small-head spines (Small: Control, 0.41; DHT, 0.42; T, 0.63; E2, 0.75), middle-head spines (Middle: Control, 0.33; DHT, 0.45; T, 0.35; E2, 0.40), and large-head spines (Large: Control, 0.25; DHT, 0.37; T, 0.32; E2, 0.19). (*D*) The same experimental data analyzed by Neurolucida. Abbreviations are the same as in (*C*). Spine density (spines/μm) of each subclass is as follows: small-head spines (Small: Control, 0.40; DHT, 0.42; T, 0.62; E2, 0.72), middle-head spines (Middle: Control, 0.35; DHT, 0.46; T, 0.37; E2, 0.40), and large-head spines (Large: Control, 0.26; DHT, 0.37; T, 0.32; E2, 0.19). In (*A*), (*C*), and (*D*) results are reported as mean ± standard error of the mean. Statistical significance was examined using Tukey–Kramer post hoc multiple comparisons test when one-way ANOVA tests yielded $P < 0.05$. $^{*}P < 0.05$, $^{**}P < 0.01$ versus Control. For each experimental condition, we investigated approximately 5 rats, 15 slices, 30 neurons, 60 dendrites and roughly 3500 spines.

investigate multiple pathways in systematic fashion to reveal entire molecular underpinnings of spinogenesis.

Application of Spiso-3D for the Analysis of Abnormal Spines

Various spinal abnormalities are described in human neuopsychiatric disorders (Williams et al. 1980; Hinton et al. 1991) or genetically manipulated mice (Bhatt et al. 2009) (see Supplementary Fig. S3). For example, in fragile X syndrome, spine neck length is elongated roughly 3- to 8-fold (Hinton et al. 1991), while overexpression of the structural protein drebrin resulted in a loss of spine heads and roughly 2- to 4-fold increase in spine neck length (Mizui et al. 2005). Furthermore, LIM kinase knockout mice were found to have roughly 50–60% reduction in spine-head size (Meng et al. 2002) (Supplementary Fig. S3). Quantitative classification of the types of spine abnormalities will contribute to the understanding of the mechanisms of spine formation and/or maintenance as well as potentially aid in the development of therapeutic interventions for psychiatric illnesses. However, to date, few studies quantitatively investigated these spine abnormalities, partly due to the lack of a systematic analysis method such as Spiso-3D, which allows the efficient analysis of large sets of data.

Conclusion

We achieved construction of automated software, Spiso-3D, which is effective in precise and quantitative dendritic spine analysis. The software determines spines using not only brightness but also geometric features of the neuronal images, leading to the accurate identification of spines. Furthermore, in comparison to currently used manual software such as Neurolucida, Spiso-3D considerably reduces human errors and experimenter labor. Using Spiso-3D, we discriminated between the different effects of steroid hormones (DHT, T, and E2) on hippocampal spinogenesis. These methods will help to analyze vast amounts of dendritic spines in neurons in the mammalian cerebral cortex.

Supplementary Material

Supplementary material can be found at: http://www.cercor.oxfordjournals.org/.

Notes

We thank Dr Anna Barron (University of Tokyo) for the critical reading of the manuscript. We appreciate S. Furuyama, H. Kawasaki, and R. Fujimura (Keio University) for developing the software. *Conflict of Interest*: None declared.

References

Al-Kofahi O, Can A, Lasek S, Szarowski DH, Turner JN, Roysam B. 2003. Algorithms for accurate 3D registration of neuronal images acquired by confocal scanning laser microscopy. J Microsc. 211:8–18.

Baulieu EE. 1997. Neurosteroids: of the nervous system, by the nervous system, for the nervous system. Recent Prog Horm Res. 52:1–32.
Bhatt DH, Zhang S, Gan WB. 2009. Dendritic spine dynamics. Annu Rev Physiol. 71:261–282.
Dima A, Scholz M, Obermayer K. 2002. Automatic segmentation and skeletonization of neurons from confocal microscopy images based on the 3-D wavelet transform. IEEE Trans Image Process. 11:790–801.
Harvey CD, Yasuda R, Zhong H, Svoboda K. 2008. The spread of Ras activity triggered by activation of a single dendritic spine. Science. 321:136–140.
Hatanaka Y, Mukai H, Mitsuhashi K, Hojo Y, Murakami G, Komatsuzaki Y, Sato R, Kawato S. 2009. Androgen rapidly increases dendritic thorns of CA3 neurons in male rat hippocampus. Biochem Biophys Res Commun. 381:728–732.
He W, Hamilton TA, Cohen AR, Holmes TJ, Pace C, Szarowski DH, Turner JN, Roysam B. 2003. Automated three-dimensional tracing of neurons in confocal and brightfield images. Microsc Microanal. 9:296–310.
Hinton VJ, Brown WT, Wisniewski K, Rudelli RD. 1991. Analysis of neocortex in three males with the fragile X syndrome. Am J Med Genet. 41:289–294.
Hojo Y, Hattori TA, Enami T, Furukawa A, Suzuki K, Ishii HT, Mukai H, Morrison JH, Janssen WG, Kominami S, et al. 2004. Adult male rat hippocampus synthesizes estradiol from pregnenolone by cytochromes P45017alpha and P450 aromatase localized in neurons. Proc Natl Acad Sci U S A. 101:865–870.
Kawato S, Hojo Y, Kimoto T. 2002. Histological and metabolism analysis of P450 expression in the brain. Methods Enzymol. 357:241–249.
Kopec CD, Real E, Kessels HW, Malinow R. 2007. GluR1 links structural and functional plasticity at excitatory synapses. J Neurosci. 27:13706–13718.
Kretz O, Fester L, Wehrenberg U, Zhou L, Brauckmann S, Zhao S, Prange-Kiel J, Naumann T, Jarry H, Frotscher M, et al. 2004. Hippocampal synapses depend on hippocampal estrogen synthesis. J Neurosci. 24:5913–5921.
Krissian K, Malandain G, Ayache N. 2000. Model-based detection of tubular structures in 3D images. Comput Vision Image Understand. 80:130–171.
Lindeberg T. 1990. Scale-space for discrete signals. IEEE Trans Pattern Anal Machine Intell. 12:234–253.
Matsuzaki M, Honkura N, Ellis-Davies GC, Kasai H. 2004. Structural basis of long-term potentiation in single dendritic spines. Nature. 429:761–766.
Meng Y, Zhang Y, Tregoubov V, Janus C, Cruz L, Jackson M, Lu WY, MacDonald JF, Wang JY, Falls DL, et al. 2002. Abnormal spine morphology and enhanced LTP in LIMK-1 knockout mice. Neuron. 35:121–133.
Mizui T, Takahashi H, Sekino Y, Shirao T. 2005. Overexpression of drebrin A in immature neurons induces the accumulation of F-actin and PSD-95 into dendritic filopodia, and the formation of large abnormal protrusions. Mol Cell Neurosci. 30:149–157.
Mukai H, Tsurugizawa T, Murakami G, Kominami S, Ishii H, Ogiue-Ikeda M, Takata N, Tanabe N, Furukawa A, Hojo Y, et al. 2007. Rapid modulation of long-term depression and spinogenesis via synaptic estrogen receptors in hippocampal principal neurons. J Neurochem. 100:950–967.
Murakami G, Tsurugizawa T, Hatanaka Y, Komatsuzaki Y, Tanabe N, Mukai H, Hojo Y, Kominami S, Yamazaki T, Kimoto T, et al. 2006. Comparison between basal and apical dendritic spines in estrogen-induced rapid spinogenesis of CA1 principal neurons in the adult hippocampus. Biochem Biophys Res Commun. 351:553–558.
Ogiue-Ikeda M, Tanabe N, Mukai H, Hojo Y, Murakami G, Tsurugizawa T, Takata N, Kimoto T, Kawato S. 2008. Rapid modulation of synaptic plasticity by estrogens as well as endocrine disrupters in hippocampal neurons. Brain Res Rev. 57:363–375.
Rodriguez A, Ehlenberger DB, Dickstein DL, Hof PR, Wearne SL. 2008. Automated three-dimensional detection and shape classification of dendritic spines from fluorescence microscopy images. PLoS ONE. 3:e1997.
Schmitt S, Evers JF, Duch C, Scholz M, Obermayer K. 2004. New methods for the computer-assisted 3-D reconstruction of neurons from confocal image stacks. Neuroimage. 23:1283–1298.
Shinohara Y, Hirase H, Watanabe M, Itakura M, Takahashi M, Shigemoto R. 2008. Left-right asymmetry of the hippocampal synapses with differential subunit allocation of glutamate receptors. Proc Natl Acad Sci U S A. 105:19498–19503.
Streekstra GJ, van Pelt J. 2002. Analysis of tubular structures in three-dimensional confocal images. Network. 13:381–395.
van Pelt J, van Ooyen A, Uylings HB. 2001. The need for integrating neuronal morphology databases and computational environments in exploring neuronal structure and function. Anat Embryol (Berl). 204:255–265.
Wearne SL, Rodriguez A, Ehlenberger DB, Rocher AB, Henderson SC, Hof PR. 2005. New techniques for imaging, digitization and analysis of three-dimensional neural morphology on multiple scales. Neuroscience. 136:661–680.
Williams RS, Hauser SL, Purpura DP, DeLong GR, Swisher CN. 1980. Autism and mental retardation: neuropathologic studies performed in four retarded persons with autistic behavior. Arch Neurol. 37:749–753.